JOURNAL OF GEOPHYSICAL RESEARCH: OCEANS, VOL. 118, 6791–6806, doi:10.1002/jgrc.20400, 2013

Poleward propagating subinertial alongshore surface currents off the U.S. West Coast

Sung Yong Kim,[1] Bruce D. Cornuelle,[2] Eric J. Terrill,[3] Burt Jones,[4] Libe Washburn,[5] Mark A. Moline,[6] Jeffrey D. Paduan,[7] Newell Garfield,[8] John L. Largier,[9] Greg Crawford,[10] and P. Michael Kosro[11]

Received 5 June 2013; revised 11 September 2013; accepted 12 September 2013; published 12 December 2013.

[1] The network comprising 61 high-frequency radar systems along the U.S. West Coast (USWC) provides a unique, high resolution, and broad scale view of ocean surface circulation. Subinertial alongshore surface currents show poleward propagating signals with phase speeds of $O(10)$ and $O(100–300)$ km d^{-1} that are consistent with historical in situ observations off the USWC and that can be possibly interpreted as coastally trapped waves (CTWs). The propagating signals in the slow mode are partly observed in southern California, which may result from scattering and reflection of higher-mode CTWs due to curvature of shoreline and bathymetry near Point Conception, California. On the other hand, considering the order of the phase speed in the slow mode, the poleward propagating signals may be attributed to alongshore advection or pressure-driven flows. A statistical regression of coastal winds at National Data Buoy Center buoys on the observed surface currents partitions locally and remotely wind-forced components, isolates footprints of the equatorward propagating storm events in winter off the USWC, and shows the poleward propagating signals year round.

Citation: Kim, S. Y., et al. (2013), Poleward propagating subinertial alongshore surface currents off the U.S. West Coast, *J. Geophys. Res. Oceans*, *118*, 6791–6806, doi:10.1002/jgrc.20400.

1. Introduction

[2] Surface current measurements using shore-based high-frequency radars (HFRs) have matured as an observational tool in coastal oceanography [e.g., *Paduan and Cook*, 1997; *Shay*, 1997]. High-resolution time series of surface current maps (kilometer in space and hourly in time) over a coastal region have become resources for research and education as well as decision making and policy. The HFR network deployed on the U.S. West Coast (USWC) has provided a framework to examine coastal surface circulation from submesoscale to mesoscale [e.g., *Kim et al*., 2011]. These features include poleward or equatorward propagating features near the coast, near-inertial surface currents, surface tide-coherent currents, local and remote wind-coherent surface circulation, intermittent and persistent submesoscale and mesoscale eddies, and surface features of internal waves and tides.

[3] Poleward propagating subinertial signals along the coast have been described within the dynamical framework of coastal trapped waves (CTWs) [e.g., *Allen*, 1980; *Chapman*, 1987; *Ramp et al*., 1997]. CTWs have time scales longer than the inertial period (between a few days and a few weeks) and propagate with the coast on the right (left) in the northern (southern) hemisphere. The CTWs are considered as a hybrid of barotropic continental shelf waves (homogeneous ocean and shelf topography) [e.g., *Robinson*, 1964; *Rhines*, 1970] and internal Kelvin waves (stratified ocean and no-bottom topography) [e.g., *Fjeldstad*, 1933; *Charney*, 1955]. The Burger number (B) distinguishes these two characteristics as the ratio of the (baroclinic) Rossby deformation radius ($R = NH/f_c$) to the horizontal length scale under an assumption of finite H/L;

$$B = \left(\frac{R}{L}\right)^2 = \left(\frac{NH}{f_c L}\right)^2, \quad (1)$$

[1]Division of Ocean Systems Engineering, School of Mechanical, Aerospace and Systems Engineering, Korea Advanced Institute of Science and Technology, Daejeon, Republic of Korea.
[2]Climate, Atmospheric Science and Physical Oceanography, Scripps Institution of Oceanography, La Jolla, California, USA.
[3]Marine Physical Laboratory, Scripps Institution of Oceanography, La Jolla California, USA.
[4]Red Sea Research Center, King Abdullah University of Science and Technology, Thuwal, Saudi Arabia.
[5]Department of Geography/ICESS, University of California, Santa Barbara, Santa Barbara, California, USA.
[6]School of Marine Science and Policy, College of Earth, Ocean, and Environment, University of Delaware, Newark, Delaware, USA.
[7]Department of Oceanography, Graduate School of Engineering and Applied Sciences, Naval Postgraduate School, Monterey, California, USA.
[8]Geosciences Department and Romberg Tiburon Center for Environmental Studies, San Francisco State University, Tiburon, California, USA.
[9]Bodega Marine Laboratory, University of California, Davis, Bodega Bay, California, USA.
[10]Faculty of Science and Technology, Vancouver Island University, Nanaimo, British Columbia, Canada.
[11]College of Earth, Ocean, and Atmospheric Sciences, Oregon State University, Corvallis, Oregon, USA.

Corresponding author: S. Y. Kim, Division of Ocean Systems Engineering, School of Mechanical, Aerospace and Systems Engineering, Korea Advanced Institute of Science and Technology, 291 Daehak-ro, Yuseong-gu, Daejeon 305–701, Republic of Korea. (syongkim@kaist.ac.kr)

2169-9275/13/10.1002/jgrc.20400

Table 1. Chronological Observations of Poleward Currents on the USWC, presented with their Magnitudes ($|\mathbf{u}|$, cm s^{-1}), Propagation Speeds ($C_\mathbf{u}$, km d^{-1}) (for Three Modes if Applicable) and Periods (T, days), Study Periods and Areas, and Applied Analyses[a]

Observations	$\|\mathbf{u}\|$	$C_\mathbf{u}$	T	Study Period	Study Area	Analysis
Halliwell and Allen [1984]		325		CODE-1,-2	USWC (32°N–48°N)	TSA/EOF
Battisti and Hickey [1984]		500 1600 900		Jul 1972 to Sep 1972 Jan 1977 to Mar 1977 Aug 1978 to Oct 1978	OR, WA (43°N–48°N)	LCTWM/TSA
Spillane et al. [1987]		150–200	50	Apr 1971 to Apr 1975	E. Pacific (12°S–54°N)	TSA
Denbo and Allen [1987]		302–518		CODE-1,-2	USWC (32°N–48°N)	EOF
Wichham et al. [1987]	10–15			Jun 1978 to Jun 1980	C. CA (35.5°N–36°N)	TSA
Chapman [1987]		294–320 (1st) 143–160 (2nd) 83–90 (3rd)		CODE-1,-2	CODE region (38.5°N)	LCTWM
Chelton et al. [1988]	10–20	151–177 (possibly 2nd)		Mar 1984 to Aug 1984	C. CA (34.5°N–37.5°N)	MR
Davis and Bogden [1989]		151–237		CODE-1,-2	CODE region (38.5°N)	EOF
Ramp et al. [1997]	20–40	302 (1st) 140 (2nd) 64 (3rd)	29	May 1989 to Apr 1991	C. CA (34.6°N–38°N)	LCTWM
Auad and Hendershott [1997]		70 (possibly 3rd)	13.6	Jan 1984 to Jun 1984	S. CA (33.5°N–34.7°N)	EOF/TSA
Pierce et al. [2000] *Agostini et al*. [2006]	10–20			Jul 1995 to Aug 1995 Jul 1998 to Aug 1998	N. Pacific (33°N–51°N)/NMFS	TSA
Kosro [2002]	30–50	186		Apr 1997 to Aug 1999	CA and Oregon (32°N–45°N)	TSA
Hickey et al. [2003]		121–225		Feb 1998 to Sep 1998	S. CA (33.5°N–34.3°N)	TSA
Lavin et al. [2006]	15–30			Jun 2003, Jun 2005	SW. Mexico (17°N–23°N)	TSA
Davis et al. [2008]	5–15			CalCOFI (2005–2006)	Lines 80, 90, and 93 (30°N–35°N)	TSA
Gay and Chereskin [2009]	5–10			CalCOFI (1993–2003)	Lines 77–93 (29°N–35°N)	TSA

[a]Several analysis techniques are applied—a linear CTW model (LCTWM) [e.g., *Brink and Chapman*, 1987; *Brink*, 1990], empirical orthogonal function (EOF), multivariate regression (MR), and time series analysis (TSA) [e.g., *Emery and Thomson*, 1997]. CODE-1 and CODE-2 indicate the upwelling season (April to July) of 1981 and 1982. California Cooperative Oceanic Fisheries Investigations (CalCOFI) cruises have been conducted quarterly (January, April, July, and November). The regional acronyms of CA, OR, and WA denote California, Oregon, and Washington, respectively. Northern (N), southern (S), eastern (E), central (C), and southwestern (SW) areas are denoted with their acronyms.

where N, f_c, H, and L denote the buoyancy frequency, Coriolis frequency, the thermocline depth, and the width of the continental shelf, respectively. In weak stratification ($B \rightarrow 0$), the propagating signals resemble barotropic shelf waves, and they are similar to internal Kelvin wave-like signals under strong stratification ($B \rightarrow \infty$) [e.g., *Wang and Mooers*, 1976; *Clarke*, 1977; *Brink*, 1991]. Moreover, CTWs are influenced by changes in the waveguide due to varying stratification and bathymetry during propagation, for instance, reflection and scattering under nonadiabatic circumstances [e.g., *Miles*, 1972; *Wilkin and Chapman*, 1990].

[4] In the California Current System (CCS), the poleward currents have been identified through numerous observations (Table 1), and they are named differently depending on the variability of the California Undercurrent (CUC). The CUC is observed to flow persistently poleward over and along the continental shelf [e.g., *Sverdrup et al*., 1942; *Reid and Schwartzlose*, 1962; *Lynn and Simpson*, 1987]. The coastal (inshore) countercurrent represents the surfacing of the CUC over the shelf as a result of upwelling or positive wind stress curl [e.g., *Huyer et al*., 1989; *Ramp*, 1989]. During winter (October to February) the surface-intensified poleward current is referred to as the Davidson Current [e.g., *Reid and Schwartzlose*, 1962; *McCreary et al*., 1987; *Marchesiello et al*., 2003]. The poleward currents in the upper and inshore portion of the CCS have been observed as currents coherent with the demise or reversal of upwelling-favorable winds [e.g., *Chelton et al*., 1988; *Kosro*, 2002] and year-round currents (or surface jets) regardless of coastal wind conditions [e.g., *Steger et al*., 2000; *Garfield et al*., 2001; *Kosro*, 2005]. Turbulent processes, related to barotropic and baroclinic instability, such as fronts, jets, and submesoscale eddies in this region are attributed to (1) the instability of shear flows associated with poleward currents near the coast and equatorward California currents offshore and (2) horizontal density gradient [e.g., *Lynn and Simpson*, 1987; *Hickey*, 1998; *Marchesiello et al*., 2003]. Moreover, poleward subsurface currents, possibly the CUC, have been described as either a

spatially continuous surface jet over a long distance (from California to Oregon) or as mesoscale eddies and jets [e.g., *Collins et al*., 1996; *Garfield et al*., 1999; *Pierce et al*., 2000].

[5] Potential causes of both poleward (propagating) currents and CTWs include: alongshore atmospheric pressure setup, including upwelling-favorable winds and their relaxation or reversal [e.g., *Kosro*, 1987; *Largier et al*., 1993], positive wind stress curl with Sverdrup balance [e.g., *McCreary et al*., 1987; *Bray et al*., 1999], eddy vorticity fluxes [e.g., *Marchesiello et al*., 2003], alongshore density gradient coupled with bathymetry [e.g., *Pringle and Dever*, 2009], Kelvin wave reflection at the eastern boundary and its propagation along the coast [e.g., *Clarke*, 1983, 1982], enhanced poleward currents during El Nino–Southern Oscillation (ENSO) [e.g., *Smith*, 1983; *Huyer and Smith*, 1985; *Kosro*, 2002], and storm surge due to tropical cyclone [e.g., *Fandry et al*., 1984; *Tang and Grimshaw*, 1995].

[6] As a consequence of sparse in situ observations and overly idealized numerical models, many key questions and issues remain understating the role of CTWs in the coastal ocean dynamics and their effects on nearshore ecosystems. For example, how do the propagating low-frequency current fluctuations caused by CTWs modulate delivery of biogenic particles and other subsidies to nearshore habitats such as kelp forests? What fraction of the CTW energy flux does propagate northward around capes and headlands like Point Conception and Cape Mendocino? What role do CTWs and other propagating current features play in transmitting climate signals to shelves of the CCS and other eastern boundary current upwelling systems? In order to answer those questions and to resolve synoptic-scale propagating features, the long-term in situ observations over the continental slope, with adequate spatial resolution, are required.

[7] This paper investigates the alongshore variability of surface currents in terms of poleward and equatorward propagating signals using statistical analysis and compares the observed phase speeds of poleward signals with the results from a linear two-dimensional CTW model. As the winter storm events off the USWC tend to have equatorward propagating footprints (e.g., section 2.2 and Figure 2a), any poleward signals may not be detectable around these periods. Thus, a statistical regression using coastal winds at National Data Buoy Center (NDBC) buoys and surface currents is applied to isolate the wind-coherent and wind-incoherent features and to accentuate the poleward signals year round (section 3). The phase speeds of poleward propagating signals estimated from the linear CTW model and their geophysical conditions are presented (section 4). The final comments on poleward propagating signals and their implications are presented in section 5.

2. Summary of Observations

[8] All observations in this paper are based on hourly records, and their subinertial time series are generated by averaging these records with nonoverlapped 24 h windows.

2.1. Surface Currents

[9] An array of 61 shore-based HFRs on the USWC has been developed with collaborative efforts among multiple institutions and universities under three regional coastal ocean observing programs as part of the NOAA-funded Integrated Ocean Observing System (SCCOOS, CeNCOOS, and NANOOS; see Acknowledgment for more details). The surface currents and relevant kinematic and dynamic quantities are estimated on equally spaced grid points (6 km resolution) using optimal interpolation [e.g., *Kim et al*., 2008; *Kim*, 2010]. The surface currents along the USWC are characterized by variance in the low-frequency band ($|\sigma| \leq 0.4$ cycles per day (cpd)), enhanced variance centered at diurnal and semidiurnal tidal frequencies (K_1, M_2, and S_2), variance due to the diurnal wind and its harmonics, and the local inertial frequency ($f_c = 1.06-1.49$ cpd for 32°N–48°N) [e.g., *Kim et al*., 2011].

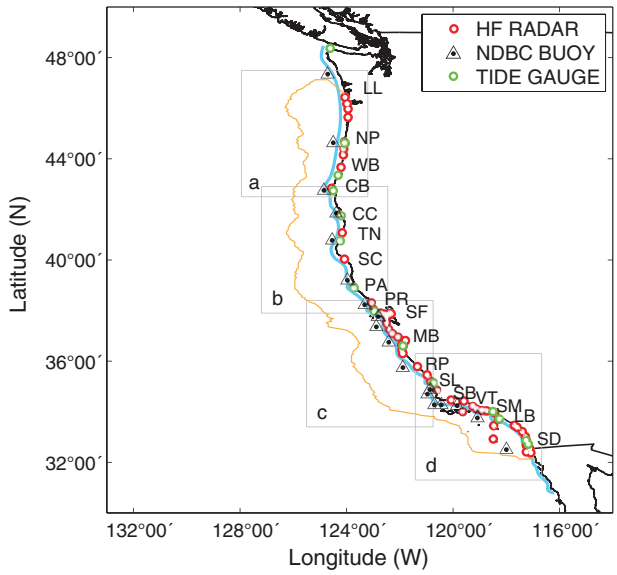

Figure 1. Surface current observations along the USWC have been conducted with 61 HFRs by multiple institutions and universities. The blue and orange curves denote the coastline axis and the effective spatial coverage of the USWC HFRs. The USWC is divided into four coastal regions with the same size for detailed spatial maps: (a) southern Washington and Oregon, (b) southern Oregon and northern California, (c) central California, and (d) southern California. For regional reference, the locations of some coastal regions along the USWC are denoted by abbreviated two letter names: San Diego (SD), Long Beach (LB), Santa Monica (SM), San Buenaventura (VT), Santa Barbara (SB), Port San Luis (SL), Ragged Point (RP), Monterey Bay (MB), San Francisco (SF), Point Reyes (PR), Point Arena (PA), Shelter Cove (SC), Trinidad (TN), Crescent City (CC), Cape Blanco (CB), Winchester Bay (WB), Newport (NP), and Loomis Lake (LL).

[10] In order to present the alongshore surface currents effectively, we defined a coastline-following axis at an offshore distance of 15–20 km using a spline curve fit on grid points with a 20 km resolution [e.g., *Kim et al*., 2011]. This distance is chosen so that the axis passes through the Santa Barbara Channel (SBC) and the San Pedro Channel off southern California (Figure 1) and because the poleward flow is expected to exist within the first baroclinic Rossby

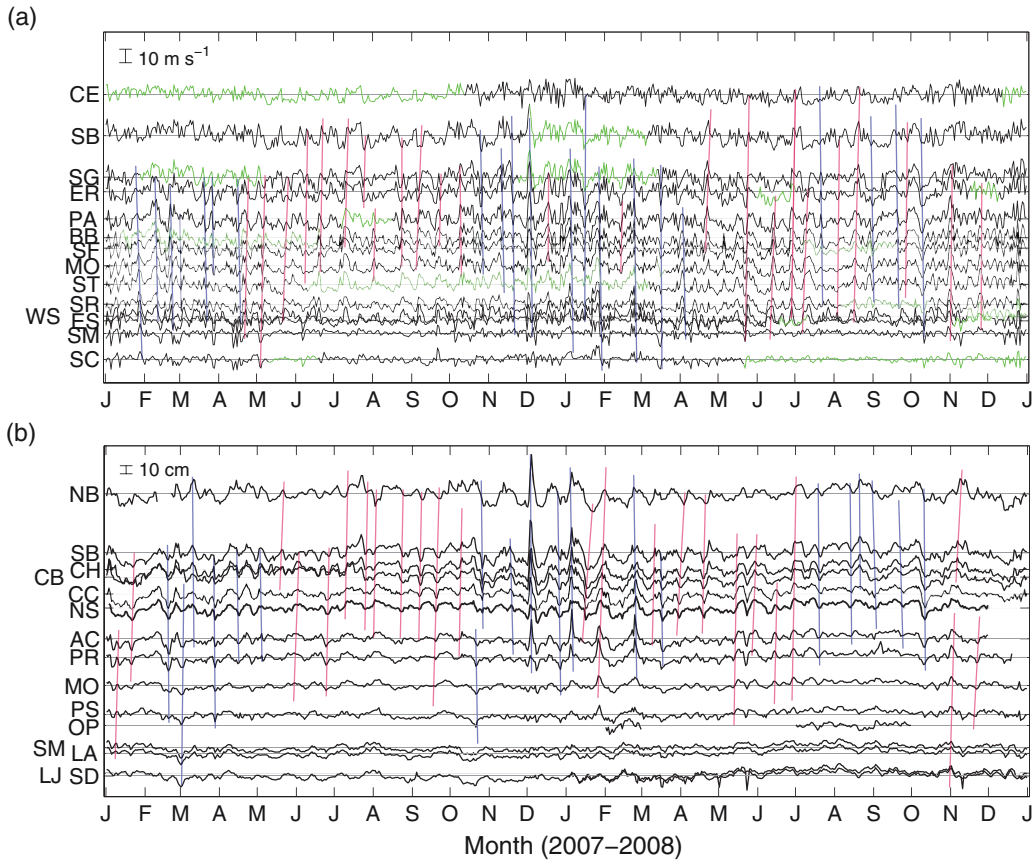

Figure 2. Time series of the anomalies of (a) subinertial alongshore winds at NDBC buoys and (b) subinertial detided sea surface heights at tide gauges off the USWC. Anomaly indicates the deviation from 2 year mean. The horizontal gray line is the reference of each time series after subtracting the 2 year mean. The poleward and equatorward propagating signals are highlighted with red and blue lines, respectively. The wind data are gap filled using the sample covariance matrix of 14 NDBC wind buoys off the USWC for 14 year records (1995–2008), indicated as green curves. The ordinate is scaled by the distance along the coast. For regional reference, the locations of NDBC buoys and tide gauges on the USWC are denoted by abbreviated two letter names: San Clemente (SC), Santa Monica (SM), East Santa Barbara (ES), West Santa Barbara (WS), Santa Maria (SR), San Martin (ST), Monterey Bay (MO), San Francisco (SF), Bodega Bay (BB), Point Arena (PA), Eel River (ER), Saint George (SG), Stonewall Bank (SB), and Cape Elizabeth (CE), respectively, San Diego (SD), La Jolla (LJ), Los Angeles (LA), Santa Monica (SM), Oil Platform Harvest (OP), Port San Luis (PS), Monterey (MO), Point Reyes (PR), Arena Cove (AC), North Spit (NS), Crescent City (CC), Cape Blanco (CB), Charleston (CH), South Beach (SB), and Neah Bay (NB). The first day of each month is labeled.

deformation radius in a range of 15–30 km (32–48°N) [e.g., *Stammer*, 1997; *Chelton et al*., 1998; *Huyer*, 1990] (see sections 3.1 and 4). In this paper, the surface currents along this coastline axis are computed from local averaging of surface currents within a 10 km radius of individual grid points on the axis. The alongshore and cross-shore current components of surface currents are defined as the parallel and normal components to the coastline axis, respectively. However, the wind transfer functions and response functions are estimated without any rotation of either winds or surface currents in order to use a consistent directional convention and to avoid ambiguity between veering angle and phase (section 3.2). The USWC is divided into four subregions of similar size to show detailed surface current maps (e.g., Figure 7): southern Washington and Oregon (region a), southern Oregon and northern California (region b), central California (region c), and southern California (region d).

2.2. Coastal Surface Winds and Sea Surface Heights

[11] The coastal surface winds observed at 14 NDBC buoys and the atmospherically adjusted [e.g., *Agnew*, 1986; *Wunsch and Stammer*, 1997] hourly sea surface heights (SSHs; η) recorded relative to the North American Vertical Datum (NAVD) at 14 tide gauges for 2 years (2007 and 2008) are used to examine the relevant alongshore variability and propagating signals (Figure 1). If wind and SSH data have sparse temporal data availability and show inconsistency with data at other stations, they are excluded. In a similar way, the shore-based wind observations from the Coastal Marine Automated Network (C-MAN), National Estuarine Research Reserve System (NERRS), and Coastal Data Information Program (CDIP) are not used because the regional influence imposed on the data and the inconsistency in the large scale variability are

not appropriate for this analysis. The basic statistics of coastal winds and SSHs are also described elsewhere [e.g., *Dorman and Winant*, 1995; *García-Reyes and Largier*, 2010].

[12] The time series of subinertial alongshore surface winds and detided sea surface heights (SSH anomalies; SSHAs) for 2 years (2007 and 2008) are shown in Figure 2. The alongshore wind is defined as the component parallel to the principal axis of the subinertial wind instead of the local slope of the shoreline because the principal axis captures the directional preference of subinertial variability better and the local slope of the shoreline may have a bias in the estimate. Poleward and equatorward propagating signals are highlighted with red and blue lines, respectively. Although propagating features in both time series are not always coherent, they typically appear in summer (poleward) and winter-spring (equatorward) with time intervals of 10–30 days between propagating events and durations of 5–10 days in a single event. Those periods are related in part to the well-known seasonal variability off the USWC, which include upwelling-favorable winds in spring, their relaxation in summer/fall, and winter storms initiated from the northern end of the west coast region. The order of phase speeds of equatorward and poleward signals are $O(100)$ and $O(100–1000)$ km d^{-1}, respectively.

[13] The wind in the coastal region is characterized by a combination of large scale, subdiurnal winds, and local diurnal land/sea breezes. The alongshore wind is considered to be more effective driving force in subinertial coastal circulation than the cross-shore wind [e.g., *Csanady*, 1982; *Brink et al*., 1987]. The subdiurnal wind on the USWC contains 50%–80% of the total variance, and the diurnal wind and its harmonics account for 10%–25% of the total variance. The variance of the diurnal wind can be inversely correlated with the distance from the coast [e.g., *Brink and Muench*, 1986]. Although *Chapman* [1987] applied a scale factor ($\sim$1.35) between the coastal wind at the shore station and offshore wind at the buoy, the scale factor is not used in this analysis because the subdiurnal winds are dominant contributors in variance and they have the spatial consistency in the amount of variance.

[14] The wind regression on the surface currents (section 3) can be sensitive to the data quality (e.g., fraction of missing observations) and the signal-to-noise ratio (SNR) in the data (e.g., the variance ratio of alongshore wind and cross-shore wind). Thus, wind data are gap filled using the sample covariance matrix of 14 NDBC wind buoys off the USWC for 14 year records (1995–2008), and they are converted into wind stress using the drag coefficient formulation described in *Yelland and Taylor* [1996]. The only gap-filled time series are presented as green curves in Figure 2a. On the other hand, surface currents are not gap filled because a statistically stable sample covariance matrix can not be constructed from available surface current observations due to missing data in northern California for about 1 year (e.g., regions between PA and CC in Figure 4a).

2.3. Bathymetry

[15] The bathymetric data (ETOPO2v2), with a 2 min grid resolution, is provided by National Geophysical Data Center (NGDC) [*National Geophysical Data Center*, 2006]. A coast-following bathymetry on the USWC is derived from local depth profiles on the offshore lines normal to the coastline axis from the coast to 120 km offshore (Figure 3a). For an appropriate presentation of bathymetry, the aspect ratio of Figure 3a was modified (the actual aspect ratio is 0.12). A thick contour indicates 200 m water depth as a typical continental shelf boundary. The representation of islands becomes somewhat distorted; islands are larger or smaller, depending on whether the local coastline is concave or convex, respectively. The variation of bottom topography in the alongshore direction (e.g., the width of continental shelf) can cause the propagating waves and signals to scatter and reflect [e.g., *Webster*, 1987; *Wilkin and Chapman*, 1990]. Figure 3b showed the alongshore distribution of phase speeds estimated from a linear two-dimensional CTW model, discussed in section 4.

3. Statistical Model

[16] Coastal surface currents are considered as mixed responses to oceanographic and meteorological forces (e.g., surface tides, winds, alongshore pressure gradients) and their nonlinear interactions. The driving forces can comprise several component(s) depending on the study area [e.g., *Kim et al*., 2010a]. Their decomposition, based on relevant forcing mechanisms, enables us to understand the physical characteristics of individual current components.

[17] In this analysis, (total) surface currents ($\mathbf{u}$) are decomposed into purely tide coherent ($\mathbf{u}_T$) and detided surface currents ($\mathbf{u}_F$) by removing components at tidal constituents frequencies using a least-squares fit. Then, the locally wind-coherent currents ($\mathbf{u}_W$) are extracted from the detided surface currents ($\mathbf{u}_F$), using the wind response function, to accentuate the propagating features. The wind regression in the time domain, equivalent to the transfer function analysis in the frequency domain, isolates the wind-coherent components [e.g., *Kim et al*., 2009a]. Finally, the residual surface currents ($\mathbf{u}_R$) include wind incoherent, baroclinic tidal and nonlinearly modulated tidal components, and intermittent and persistent eddies:

$$\mathbf{u} = \mathbf{u}_T + \mathbf{u}_F = \mathbf{u}_T + \mathbf{u}_W + \mathbf{u}_R. \quad (2)$$

[18] In a similar way as shown in section 2, the subinertial time series of individual components (e.g., $\mathbf{u}_W$ and $\mathbf{u}_R$) are computed by averages using nonoverlapped 24 h time windows.

3.1. Detided Surface Currents

[19] A time-alongcoast plot of subinertial alongshore surface currents ($\mathbf{u}_F$) for 2 years is shown in Figure 4a. The data show the poleward signals on the USWC with phase speeds of $O(10)$ and $O(100–300)$ km d^{-1} and the distinct seasonal transitions between April and June of the year due to upwelling-favorable winds and their relaxation (Figure 4a). The propagation features with slower (higher mode) phase speed ($O(10)$ km d^{-1}) are partly observed in the southern California region (from SD to SB). As higher-mode CTWs can be more sensitive to bathymetric changes and coastline curvature than lower-mode ones, they are more likely to be reflected and scattered near Point Conception, California. On the other hand, the poleward

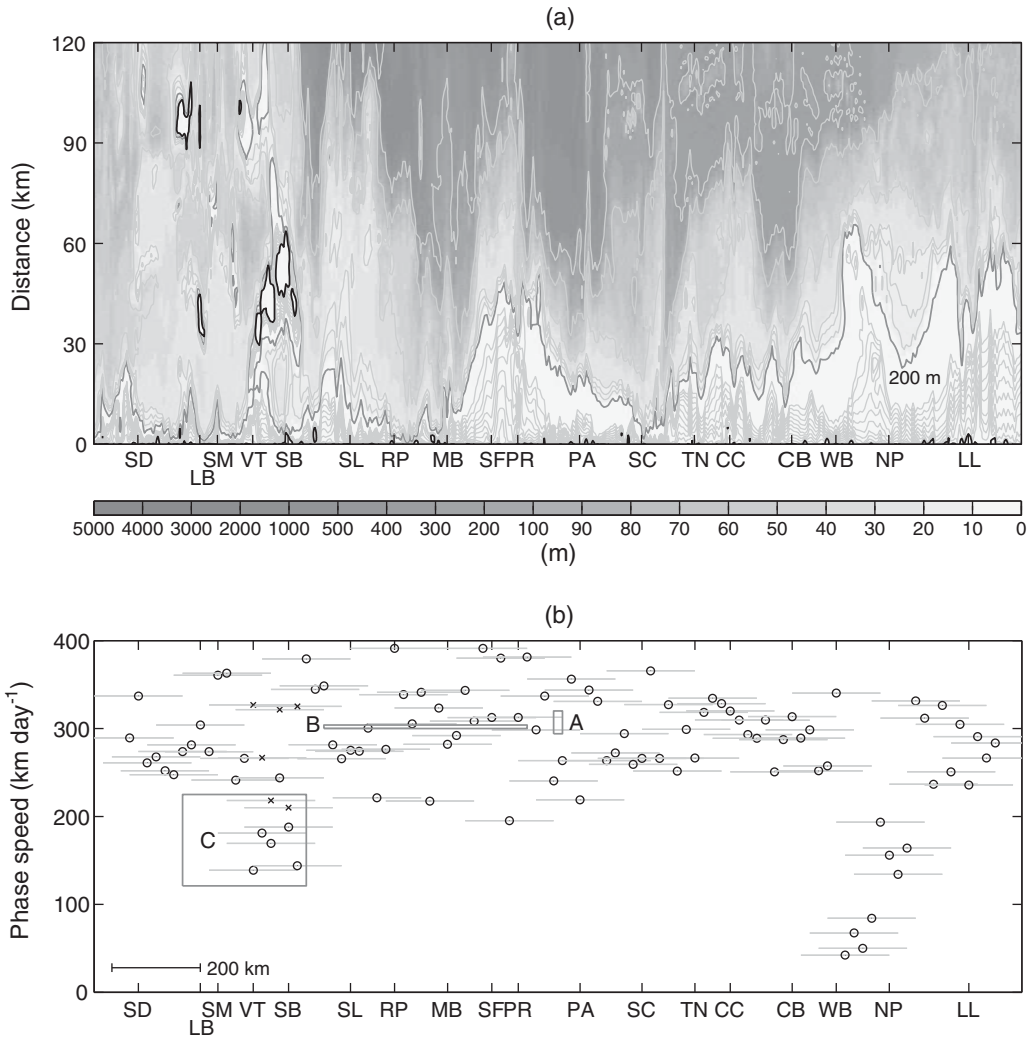

Figure 3. (a) Coast-following bathymetry on the USWC (the actual aspect is equal to 0.12). The bottom bathymetry contours are indicated by the light thin curves with 10 ($0 < z < 100$ m), 100 ($100 < z < 500$ m), and 1000 m ($1000 < z < 5000$ m) contour intervals, and a dark thick curve indicates 200 m depth as a typical continental shelf bound. (b) The phase speeds of poleward signals are estimated from in situ observations (gray boxes)—A [*Chapman*, 1987], B [*Ramp et al*., 1997], and C [*Hickey et al*., 2003]—and the linear CTW model (a circle or cross for the first mode phase speed and a horizontal line for the errorbar, assumed as approximately 200 km) (see section 4 for more details). The cross indicates the first mode phase speed when the CTW propagates outside of the SBC.

propagating signals in the slower mode can be considered as alongshore advective processes [e.g., *Auad et al*., 2011] or pressure-driven flows [e.g., *Gan and Allen*, 2002; *Washburn et al*., 2011] based on the order of magnitude of phase speeds. The poleward propagating features are also identified beyond Point Conception, i.e., Oregon and Washington, during fall and winter. These spatially extended events may be associated with the strength of seasonal spring and fall transitions or advective processes. However, the time scales of the CTWs' generation and propagation may not support the spatial extent [e.g., *Brink et al*., 1984]. In addition, the timing of poleward propagation of detided subinertial SSHAs does not always match the timing of poleward surface currents (Figure 2b).

[20] The wavenumber-frequency domain power spectrum of subinertial alongshore surface currents ($\mathbf{u}_F$) shows a limited dispersion relationship within less than 250 km wavelength and 2.5 days period as a tilted lump of variance, nearly matched with a range of 100–300 km d^{-1} phase speed (Figure 5a). Monte Carlo simulations were performed to estimate the statistical significance of the power spectrum [e.g., *Ebisuzaki*, 1997] as follows. The model data are generated to have the same correlation at zero time lag and the same variance as observations. Then, arguments of the model data are randomized, i.e., a product of a unit random complex number, then inverse Fourier transformed. Thus, the model times series have the same correlation and variance as the original time series, but do not contain the propagating features. The two-dimensional power spectrum of the model time series can be used to define the level of significance (Figure 5d). The dominant variance in the spectra of decomposed alongshore surface

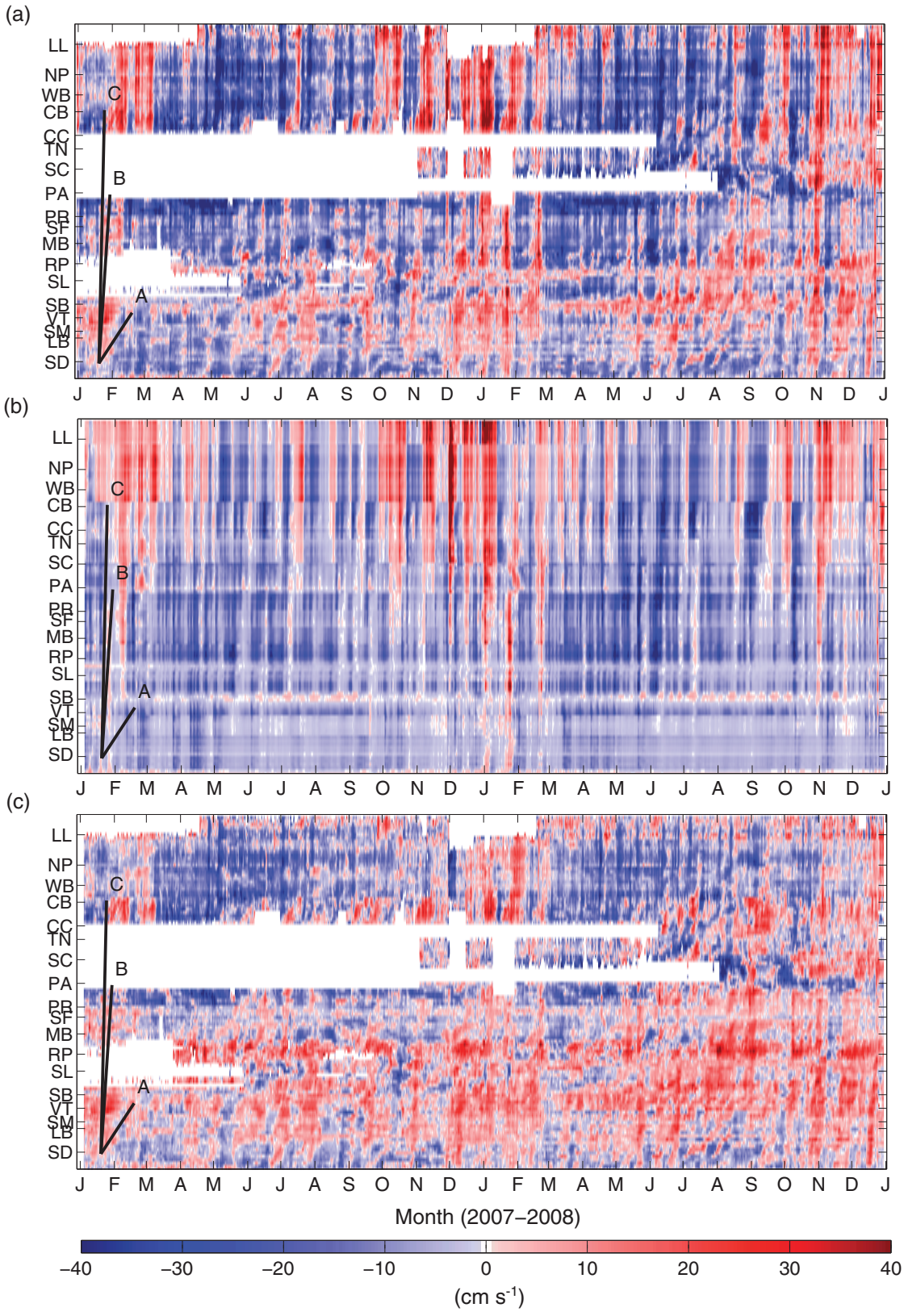

Figure 4. Time-alongcoast diagram of subinertial alongshore component (cm s^{-1}) of (a) detided surface currents ($\mathbf{u}_F$), (b) locally wind-coherent surface currents ($\mathbf{u}_W$), and (c) residual surface currents ($\mathbf{u}_R$). See Figure 1 for the abbreviated name of coastal regions. Positive currents are poleward and equatorward currents are negative. The vertical axis corresponds to the coast from San Diego to South Beach in Figure 2. Black lines indicate phase speeds of 10 (A), 100 (B), and 300 (C) km d^{-1}. The first day of each month is labeled. Figure 4a is adapted from *Kim et al*. [2011].

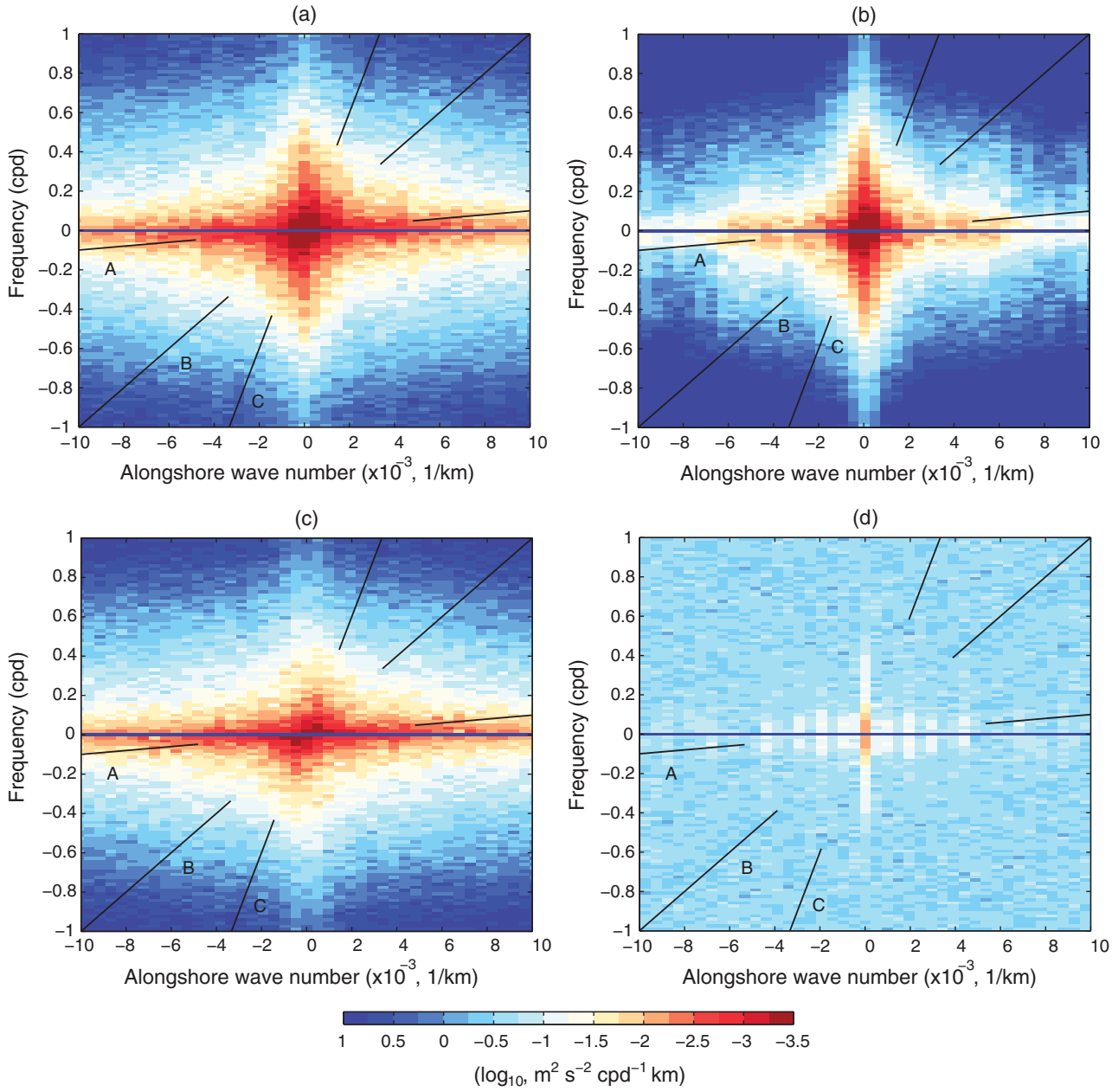

Figure 5. Two-dimensional power spectrum ($m^2\ s^{-2}\ cpd^{-1}\ km$) of (a) detided surface currents ($\mathbf{u}_F$), (b) locally wind-coherent surface currents ($\mathbf{u}_W$), (c) residual surface currents ($\mathbf{u}_R$), and (d) model surface currents simulated using Monte-Carlo method. All are plotted in log scale ($\log_{10}$). Black lines indicate phase speeds of 10 (A), 100 (B), and 300 (C) km d^{-1}.

currents ($\mathbf{u}_F$, $\mathbf{u}_W$, and $\mathbf{u}_R$) is above the significant level over much of the frequency-wavenumber domain (Figures 5a–5c, respectively, compared to Figure 5d).

[21] The time-lagged and spatial-lagged cross correlations [e.g., *Denbo and Allen*, 1987] of subinertial alongshore surface currents ($\mathbf{u}_F$) at a reference location with other regions on the USWC are considered (Figure 6). The time-lag correlation has a major peak and several minor peaks. The adjacent major peaks show a phase speed of 100–300 km d^{-1}. The minor peaks found in the southern California and Oregon areas correspond to a slow phase speed of 10–50 km d^{-1}. As described earlier, the slow phase speed can be attributed to either alongshore advection or buoyancy-driven alongshore flows considering the order of magnitude of phase speeds and the areas where minor peaks were found. However, the spread peak of correlations off Oregon may require an additional analysis in order to confirm the propagating signals in the higher mode.

[22] Figure 7 is a composite mean of surface current fields when and where poleward propagating features were identified in Figure 4a. Specifically, the poleward events were determined when (1) they appear continuously in time and space throughout the entire domain from San Diego to southern Washington and (2) their phase speeds are in the range of 100–300 km d^{-1}. Then, their alongshore

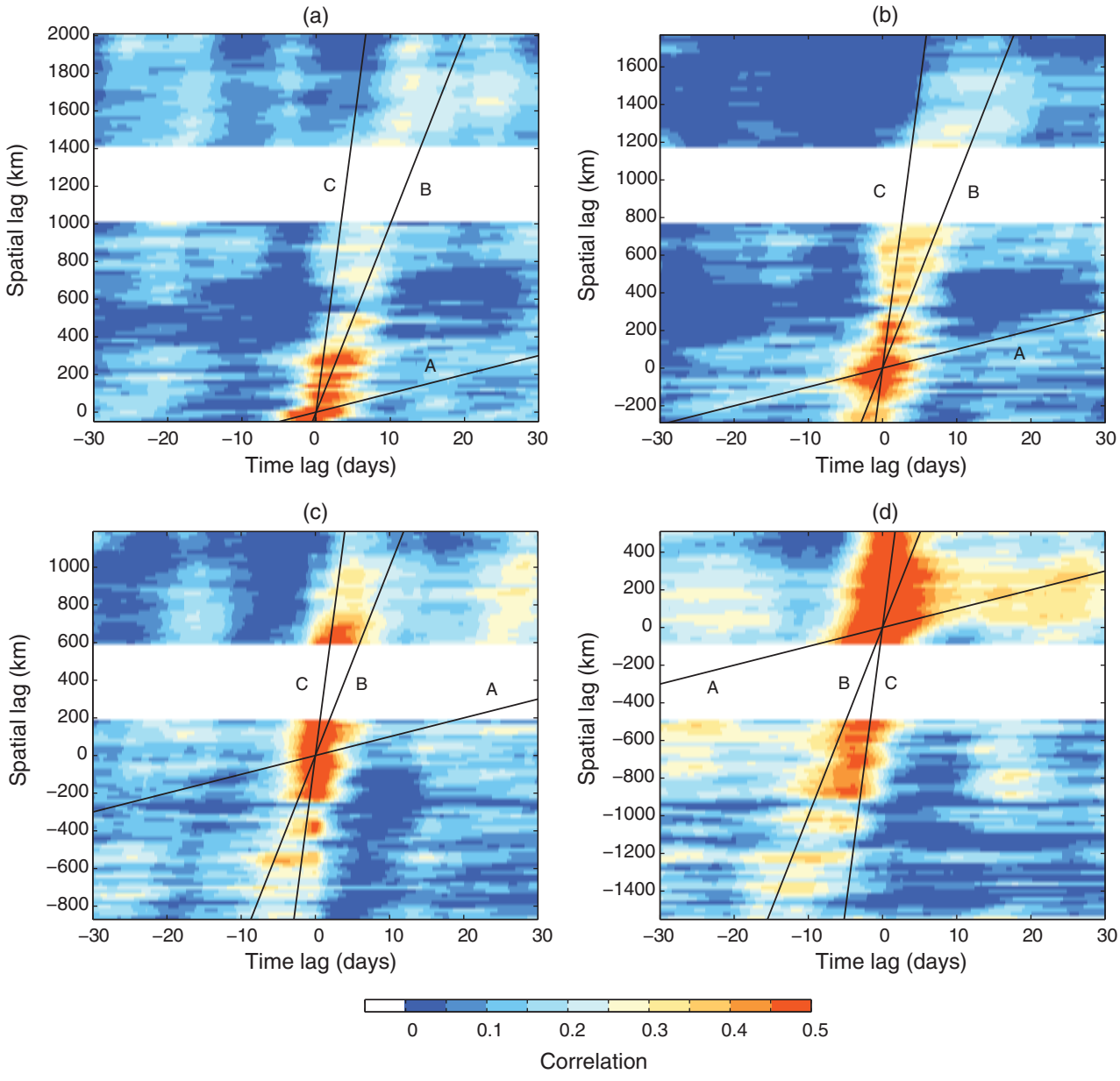

Figure 6. The time-lag and spatial-lag correlations of subinertial alongshore detided surface currents ($\mathbf{u}_F$) at a reference of (a) San Diego, (b) Santa Monica, (c) San Francisco, and (d) Port Orford. Black lines indicate phase speeds of 10 (A), 100 (B), and 300 (C) km d^{-1}. The correlation between PA and CC is excluded.

locations and time windows, considering the center of each event and its duration, are used to make a composite mean of surface current maps. This conditionally averaged surface current map shows the path of poleward propagating surface currents which appear within 30–130 km from the shoreline, shown in Figure 1 as four parts. The positive and negative values indicate the component of poleward and equatorward currents, given by the dot product of unit vectors of both surface currents and coastline axis. This composite mean suggests three regions in the cross-shore direction, embedded in the California Current surface circulation: an offshore oceanic regime ($d > 90$ km; d is the distance from the shoreline), a coastal regime ($d \leq 40$ km), and a transition zone ($40 \leq d < 90$ km) [e.g., *Kosro et al.*, 1991; *Kosro*, 2005]. The barotropic and baroclinic instability due to the shear flow and horizontal density gradient in this transition zone are thought to generate turbulent processes including submesoscale eddies on the USWC.

3.2. Wind-Coherent Surface Currents

[23] Since wind regression using the observed wind and surface currents has been addressed extensively elsewhere [e.g., *Kim et al.*, 2009a, 2010b], we briefly describe the preprocessing of observed data and provide an overview of the wind-driven current response.

[24] As discussed in *Kim et al.* [2010b], the frequency-domain transfer function and time-domain response function are complementary except for treatment of missing data. The frequency-domain transfer function is computed from a linear regression of Fourier coefficients of the time

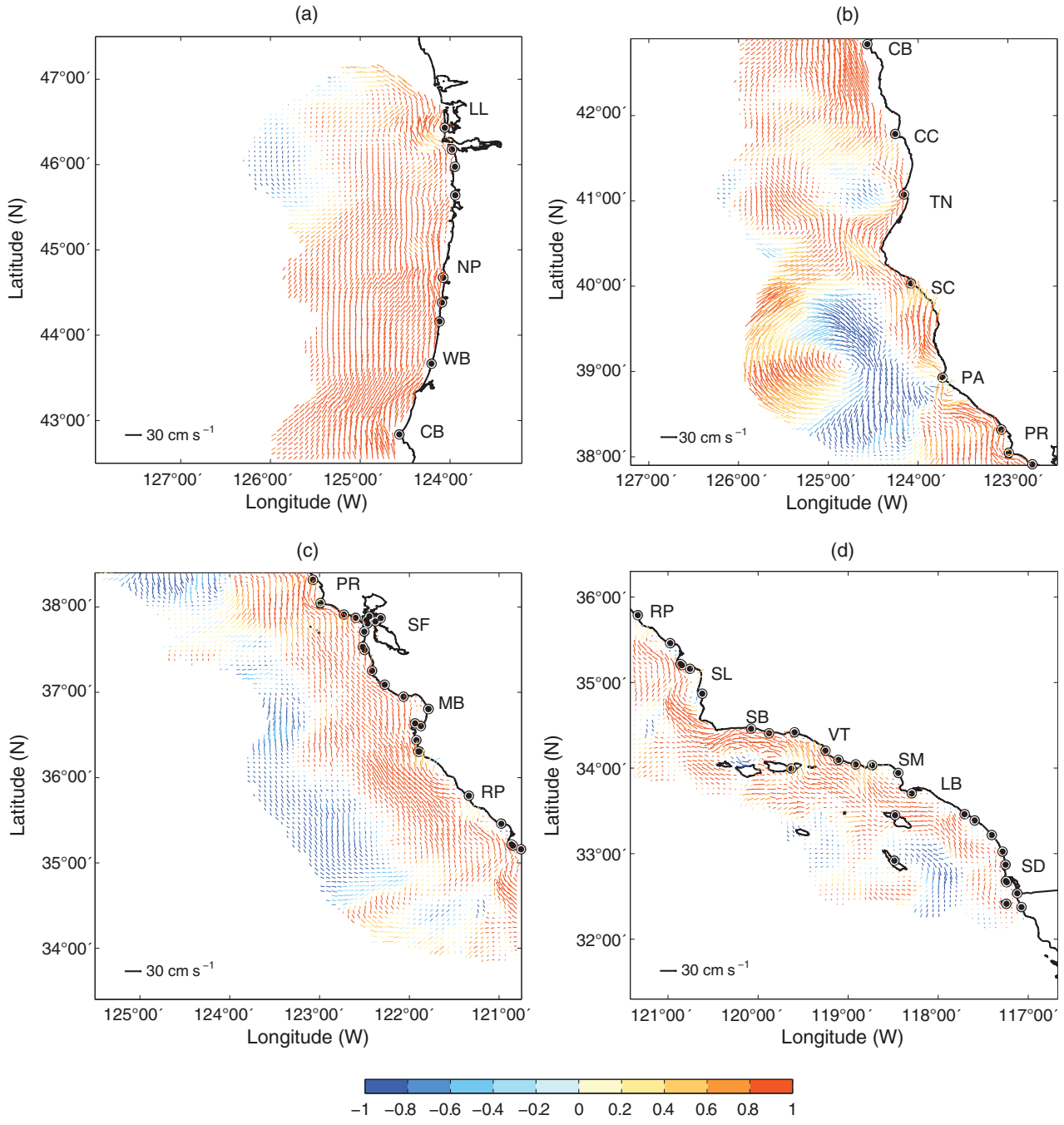

Figure 7. Surface current maps compositely averaged when poleward propagating surface currents appear. (a) Southern Washington and Oregon. (b) Southern Oregon and northern California. (c) Central California. (d) Southern California. Positive and negative values indicate the poleward and equatorward currents parallel to the coastline axis in Figure 1, respectively. See Figure 1 for the abbreviated name of coastal regions.

series divided into the same record length. If each segment does not have enough concurrent observations, that segment of data is disregarded. On the other hand, the time-domain transfer function is computed from the time-lagged wind stress and surface currents. Although the time-domain analysis can make most use of observations, the computational expense for lagged covariance is higher than frequency-domain analysis.

[25] Due to lack of concurrent observations of winds and surface currents between PA and CC, the transfer functions and wind skill in the frequency domain and the time-lagged/spatial-lagged correlations were not estimated (Figures 8 and 9). However, using multiple wind basis functions (discussed below), the impulse response function in the time domain and wind-coherent surface currents could be estimated in this area (Figure 4b).

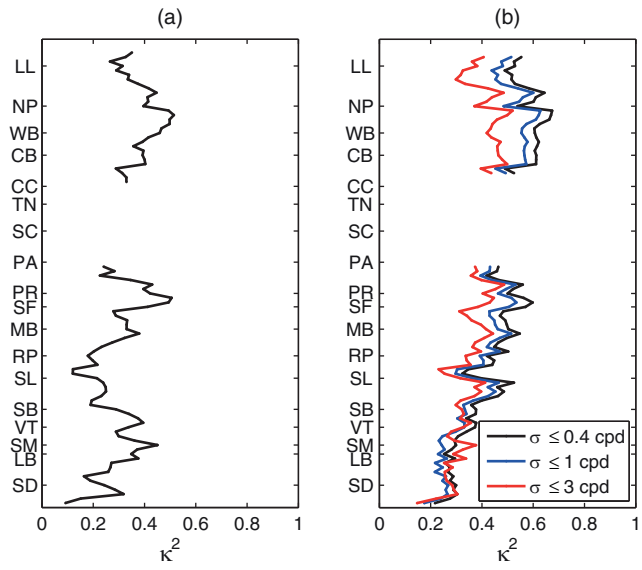

Figure 8. The fractional variance of surface currents explained by local winds—wind skill (κ^2). (a) A single wind basis within an effective frequency band ($\sigma \leq 3$ cpd) and (b) multiple wind bases are considered in the regression. Variance within three frequency bands is only counted: low frequency ($\sigma \leq 0.4$ cpd), subdiurnal ($\sigma \leq 1$ cpd), and an effective frequency band ($\sigma \leq 3$ cpd). The wind skill between PA and CC is excluded. The red curve in Figure 8b is adapted from *Kim et al*. [2011].

[26] Coastal winds are sparsely sampled in space relative to the spatial density of HFR surface currents, so a single wind time series, measured at a wind buoy, is paired with surface current measurements from a nearby location [e.g., *Kaplan et al*., 2005]. Since there is no alongshore interpolation of the wind field, the estimated transfer function can be segmented or appear discontinued.

[27] In estimating the wind impulse response function in the time domain, effective wind forcing is considered as the wind stress for 6 days prior to the surface current observation. Based on several similar wind response function analyses off the USWC, the near-inertial fluctuations decay effectively within 6 days [e.g., *Kim et al*., 2009a, 2011; *Kim and Kosro*, 2013]. The impulse response function can be interpreted as the temporal amplitudes of surface currents when the delta function wind stress is applied [*Kim and Kosro*, 2013]. On the other hand, they are the regression coefficients of time-lagged wind stress time series. In this paper, the basis functions in the wind regression are considered as the wind data in two cases such as (1) at a single wind buoy nearest where HFR surface currents are sampled and (2) at all available wind buoys off the USWC. The wind skill (κ^2), or the fraction of variance of surface currents explained by the coastal surface winds, is determined using these two different cases. Both cases show an increase in proportion to local wind forcing with a range of 0.2–0.5 from southern California to Oregon and Washington (Figure 8). The fluctuation of the wind skill partly results from the segmented response function [e.g., *Kim et al*., 2011].

[28] In the regression using multiple basis functions, the response function is computed with modified expectation maximization by applying a penalty to the error covariance matrix corresponding to the missing predictor [e.g., *Kim*, 2013]. However, the contribution of each basis function can be ambiguous without orthogonalization of basis functions. The contribution of near-inertial variance to the total wind skill is less than about 20% of the total variance depending on regional locations. Most of the wind skill is from variance at low frequency ($\sigma \leq 0.4$ cpd) (Figure 8b). When we compare the alongshore distribution of wind skills estimated in three different frequency bands ($\sigma \leq 0.4$, $\sigma \leq 1$, and $\sigma \leq 3$ cpd), the wind skill at low frequency in Oregon is more significantly reduced than the ones in southern and central California because the contribution of near-inertial variance off Oregon is dominant [e.g., *Kim and Kosro*, 2013].

3.3. Residual Surface Currents

[29] The residual surface currents ($\mathbf{u}_R$) highlight the poleward propagating signals in southern and central California, otherwise buried by the responses to upwelling-favorable (equatorward) winds (Figure 4c). These signals can be considered as remotely forced wind responses in spite of the fact that they are accompanied by some amount of noise [e.g., *Davis and Bogden*, 1989]. The two-dimensional power spectrum shows a broad dispersion relationship between phase speeds of $O(10)$ and $O(100)$ km d^{-1} (Figure 5c). Moreover, the time-lagged and spatial-lagged cross correlations of alongshore residual surface currents ($\mathbf{u}_R$) show weak yet visible propagating features compared with those of detided surface currents ($\mathbf{u}_F$) (Figure 9).

4. Linearized CTW Model

[30] A two-dimensional linearized CTW model [*Clarke and Brink*, 1985; *Brink*, 1982] provides the modal characteristics that capture the physical behaviors of CTWs. The linear CTW model was initially formulated as a two-dimensional eigenvalue problem under both the Boussinesq approximation and long-wave limit [e.g., *Gill and Schumann*, 1974]. It was subsequently improved with the implementation of a constraint of energy conservation [*Brink*, 1989] and frictional damping [*Brink*, 1990, 2006].

4.1. Formulation

[31] The linearized momentum equations with free surface, stratification [$N^2 = N^2(z)$], and topography [$h = h(z)$] are taken into account. The depth profiles normal to the coastline axis (Figure 3a) and an assumed buoyancy frequency profile are used as inputs of the model. As we assume that stratification in the upper layer has a similar shape, the vertical coordinate below the thermocline is stretched in terms of the local depth. Each run is made at every 20 km on the USWC (Figure 3b). Although this piecewise analysis can violate both assumptions of the long wave and straight coastline, the effects of bottom topography can be shown in the distribution of the phase speed in the alongshore direction. Based on repeated experiments with varying stratifications and bathymetry, the model results appear to be more sensitive to the shape of bottom bathymetry (e.g., width of the continental shelf) than to stratification. Thus, the phase speed estimates in Figure 3b may be weakly influenced by the assumed stratification.

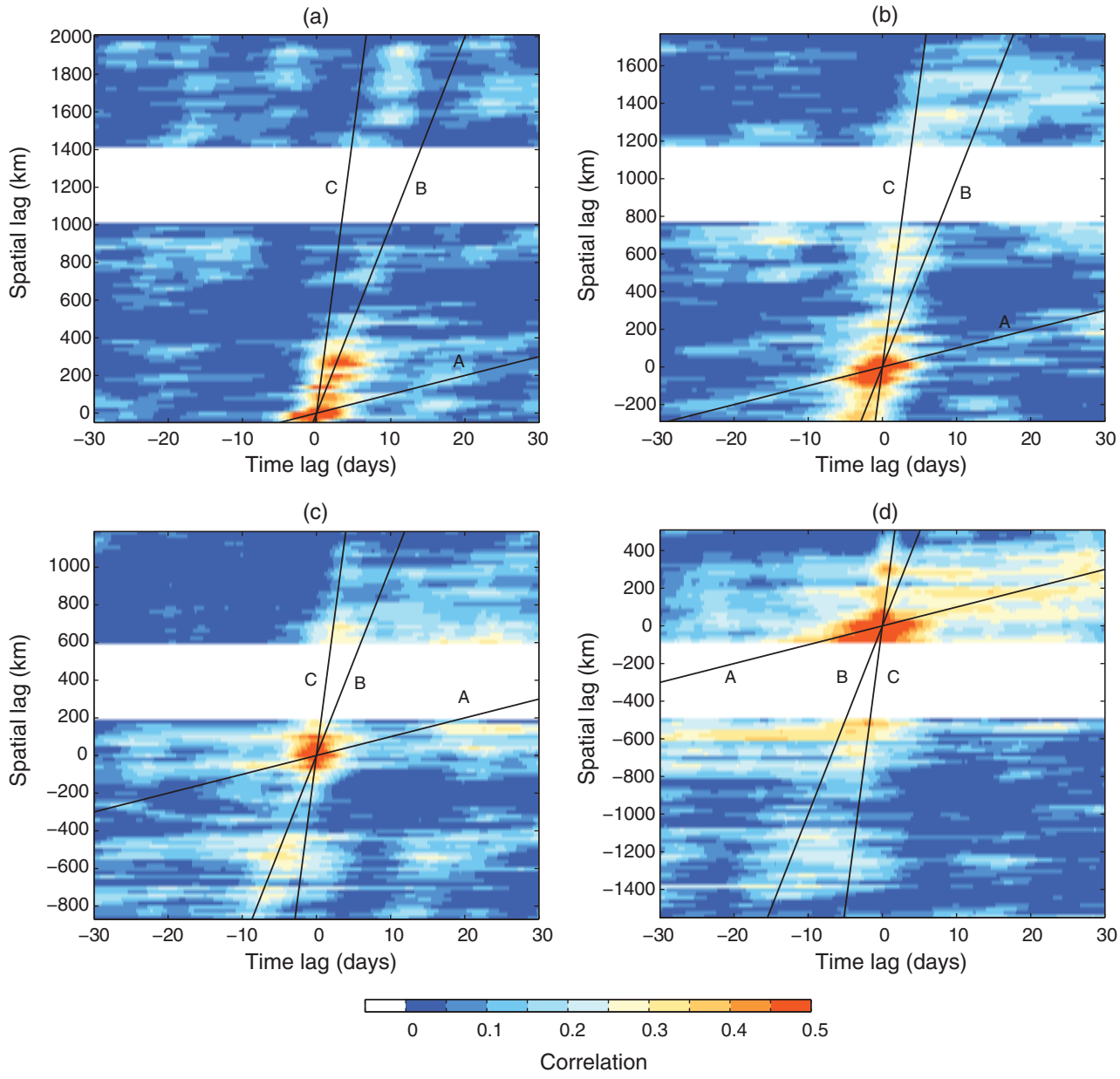

Figure 9. The time-lag and spatial-lag correlations of subinertial alongshore residual surface currents ($\mathbf{u}_R$) at the same reference location in Figure 6: (a) San Diego, (b) Santa Monica, (c) San Francisco, and (d) Port Orford. Auxiliary lines indicate phase speeds of 10 (A), 100 (B), and 300 (C) km d^{-1}. The correlation between PA and CC is excluded.

4.2. Phase Speeds

[32] A typical phase speed of the first mode CTW in the subinertial frequency band on the USWC is in a range of 250–350 km d^{-1}. The phase speed is presented as a circle (or crosses) and an errorbar with approximately 200 km long (Figure 3b). The circle and cross indicate the phase speed of two possible scenarios, corresponding to whether CTWs pass inside or outside of the SBC, respectively. CTWs are decelerated and accelerated in several coastal regions, which may result from the influence of bottom topography: 150–180 km d^{-1} in the SBC, 220–300 km d^{-1} between Point Reyes (PR) and Shelter Cove (SC), and 70–150 km d^{-1} between Winchester Bay (43.66°N) and Newport (44.67°N) off Oregon. As the solution for a specific mode may not be guaranteed for the given inputs (e.g., targeting frequency, alongshore wavenumber, bathymetry, and stratification), there is a possibility that the desired modal solution (e.g., first mode here) can be skipped. For instance, the cross-shore structures (bottom bathymetry) off Point Arena and Newport are similar but the phase speeds are quite different. Thus, the estimates with slow phase speeds at the first mode require a careful interpretation.

[33] Based on the model results for the USWC, the CTW with about 300 km d^{-1} phase speed are associated with the sea level elevation of ~10 cm and the alongshore currents of 20–30 cm s^{-1}. The phase speeds acquired from

several historical observations (Table 1) are indicated as boxes in Figure 3b, consistent and comparable with both observed poleward surface currents and model results.

[34] In addition, the coastal waves can be classified as either offshore propagating baroclinic Rossby waves or poleward propagating internal Kelvin waves, depending on their frequency and phase speed [e.g., *Grimshaw and Allen*, 1988; *Clarke and Shi*, 1991]. Thus, the observed poleward propagating signals in the paper satisfy the coastal trapping conditions off the USWC, for instance, both phase speeds of $O(10)$ and $O(100–300)$ km d^{-1} and time intervals between events of 10–30 days.

4.3. Limitations

[35] One assumption of the CTW model is that the alongshore variation of bottom topography ($\partial h/\partial l$) is negligible compared to its cross-shore gradient ($\partial h/\partial n$):

$$\frac{\partial h}{\partial l} \ll \frac{\partial h}{\partial n}. \tag{3}$$

[36] However, unless the topography is self similar, i.e., constant ratio of distance from isobaths to the coast, the incident waves will be scattered into other mode waves [e.g., *Davis*, 1983; *Wilkin and Chapman*, 1987, 1990], which might cause significant phase differences over a short distance.

[37] There are a number of regions where such limitations may apply to the two-dimensional model (e.g., northern California and Oregon) [*Battisti and Clarke*, 1982]. In addition, the dispersive effects may generate slower phase speeds than those estimated under the long-wave limit.

[38] Both amplitude and phase speed of CTWs are not easy to quantify because the density structure and bottom topography vary in space and time along the propagation path and these variations may cause the modal structure of the CTWs to vary [e.g., *Chelton and Enfield*, 1986]. However, the CTW model in this analysis is used primarily to estimate the phase speeds for given bottom bathymetry and stratification and thus to indicate that the observed poleward signals are consistent with the CTW theory.

5. Summary

5.1. Conclusions

[39] The subinertial alongshore surface currents observed from the coastal HFR network on the USWC show the poleward propagating signals with two phase speeds of $O(10)$ and $O(100–300)$ km d^{-1}, consistent with historical in situ observations within the domain. These poleward propagating features can be considered as coastally trapped waves (CTWs) — a hybrid of the barotropic continental shelf waves and internal Kelvin waves. Particularly, the propagating signals in the slow mode, partly observed in southern California, can be related to a discontinued propagation of higher-mode CTWs due to scattering and reflection at near Point Conception. On the other hand, based on the order of the slow-mode phase speed, the observed poleward signals can be attributed to the alongshore advection or pressure-driven flows.

[40] Surface tide-coherent and local wind-coherent surface currents are isolated with harmonic analysis using the least squares fit and wind regression analysis using the data-derived wind response function. The proportion of surface current variance explained by winds varies in a range of 0.2 (southern California) to 0.5 (Oregon). The wind regression using a single basis and multiple basis functions enables us to isolate the surface current responses to locally and remotely forced winds, respectively. Moreover, the residual surface currents, separated footprints of the equatorward propagating storm events in winter off the USWC, still exhibit the poleward propagating signals year round.

5.2. Discussion

[41] The wind transfer function and response function can be interpreted as a parameterization of environmental variables using regression analysis. In particular, as the regression of vector quantities can have directional dependence, i.e., anisotropy, the transfer function and response function can be estimated in isotropic and anisotropic ways [e.g., *Kim et al*., 2009a]. Moreover, as the variance of two wind components (e.g., cross-shore and alongshore winds) significantly differs, the wind regression analysis may generate a biased estimate, which can be amended with the prior information. In this paper, the isotropic response function is computed from the NDBC wind buoys and HFR-derived surface current off the USWC. The prior was chosen as the value to minimize the noise of wind observations [e.g., *Kim et al*., 2010a].

[42] A similar wind regression analysis was conducted with coastal winds at NDBC buoys and SSHs at tide gauges off the USWC [e.g., *Kim*, 2013]. Both wind-coherent and wind-incoherent SSHs have poleward propagating features, which can be considered as local and remotely forced SSH responses, respectively. Although the wind skill associated with SSHs is approximately 20% higher than the wind skill associated with surface currents, the trend of increased skills at higher latitude is consistent between SSHs and surface currents.

[43] As for the slow-mode propagating signals, three possible mechanisms were proposed such as scattered higher-mode CTWs, alongshore advection, and pressure-driven flows. Since residual surface currents, incoherent with local wind stress, contain the poleward propagating features year round, the observed signals in this paper can be explained by local and remote wind forcing and possibly local pressure-driven currents. The potential research to delineate those mixed driving forces and responses and to quantify the energy dissipation during propagation can be addressed with an adjoint method using mesoscale data-assimilated model.

5.3. Implications

[44] As described earlier, the poleward propagating signals in surface current observations appear with time intervals of 10–30 days between propagating events and durations of 5–10 days in a single event. In these time scales, the poleward signals will play a primary role to transport larvae, biogenic particles, and pollutants in the alongshore direction and to yield their settlement. Moreover, the transport of heat flux associated with alongshore

currents will deliver climate signals. Based on the wind regression analysis, the operational local and remote wind observations can be used as a predictor of the alongshore signals for some degree.

[45] The shear currents and density gradient associated with poleward currents near the coast and equatorward California currents offshore can generate eddies through the barotropic and baroclinic instability. The variability of mesoscale and submesoscale eddies may be related to the strength of poleward currents, which represents a topic for future research. Moreover, seasonal eddy generation can be considered as an influence of poleward currents—less in spring and more in winter and fall [e.g., *Kim et al*., 2011].

[46] The poleward currents in southern California appear near the coast along with a quasi-permanent counterclockwise circulation even during the period of strong upwelling-favorable (equatorward) winds [e.g., *Chelton*, 1984], which results partly from the alongshore pressure gradient and positive wind stress curl [e.g., *Hickey and Pola*, 1983; *McCreary et al*., 1987; *Bray et al*., 1999]. Moreover, inshore poleward currents developed in late summer have been reported in observations of shipboard ADCP and altimetry [e.g., *Lynn and Simpson*, 1987; *Strub and James*, 2000]. Those flows are also important for the retention of waterborne materials including nutrients, plankton, larvae and pollutants [e.g., *Wing et al*., 1995; *Kaplan et al*., 2005; *Kim et al*., 2009b].

[47] **Acknowledgments.** Sung Yong Kim is supported by the Basic Science Research Program through the National Research Foundation (NRF), Ministry of Education (no. 2013R1A1A2057849) and the Human Resources Development of the Korea Institute of Energy Technology Evaluation and Planning (KETEP), Ministry of Trade, Industry and Energy (no. 20114030200040), Republic of Korea. Data from this report originate from the following universities and research organizations on the USWC: Scripps Institution of Oceanography (SIO) at University of California, San Diego, University of Southern California, Marine Science Institute at University of California, Santa Barbara, California Polytechnic State University, Naval Postgraduate School, Romberg Tiburon Center at San Francisco State University, Humboldt State University, Bodega Marine Laboratory at University of California, Davis, and Oregon State University. Three USWC Integrated Ocean Observing System (IOOS) regional observing systems—Southern California Coastal Ocean Observing System (SCCOOS), Central and Northern California Ocean Observing System (CeNCOOS), and Northwest Association of Networked Ocean Observing System (NANOOS)—are acknowledged for their continued support and advocacy of HFR current measurements for monitoring the oceans. The majority of the HFR network was installed by the State of California's Coastal Ocean Currents Monitoring Program (COCMP) south of 41.1°N and by the Global Ocean Ecosystem Dynamics (GLOBEC) under NOAA/NSF and Research Internships in Science of the Environment (RISE) under NSF programs north of 41.1°N. The bottom bathymetry from National Geophysical Data Center (NGDC), the hourly sea surface heights from Center for Operational Oceanographic Products and Services (CO-OPS) in NOAA, and the wind and atmospheric pressure from National Data Buoy Center (NDBC) and NCEP/NCAR reanalysis are used in this study. The two-dimensional linear model for CTWs was graciously provided by Ken Brink of Woods Hole Oceanographic Institution. The order of coauthors is assigned poleward as the direction of CTWs in the northern hemisphere.

References

Agnew, D. C. (1986), Detailed analysis of tide gauge data: A case history, *Mar. Geod.*, *10*, 231–255.

Agostini, V. N., R. C. Francis, A. B. Hollowed, S. D. Pierce, C. Wilson, and A. N. Hendrix (2006), The relationship between Pacific hake (Merluccius productus) distribution and poleward subsurface flow in the California Current System, *Can. J. Fish. Aquat. Sci.*, *63*, 2648–2659, doi:10.1139/F06–139.

Allen, J. S. (1980), Models of wind-driven currents on the continental shelf, *Annu. Rev. Fluid Mech.*, *12*, 389–433.

Auad, G., and M. C. Hendershott (1997), The low-frequency transport in the Santa Barbara Channel: Description and forcing, *Cont. Shelf Res.*, *17*(7), 779–802.

Auad, G., D. Roemmich, and J. Gilson (2011), The California Current System in relation to the Northeast Pacific Ocean circulation, *Prog. Oceanogr.*, *91*(4), 576–592.

Battisti, D. S., and A. J. Clarke (1982), A simple method for estimating barotropic tidal currents on continental margins with specific application to the M2 tide off the Atlantic and Pacific Coasts of the United States, *J. Phys. Oceanogr.*, *12*(1), 8–16.

Battisti, D. S., and B. M. Hickey (1984), Application to remote wind-forced coastal trapped wave theory to the Oregon and Washington coasts, *J. Phys. Oceanogr.*, *14*, 887–903.

Bray, N. A., A. Keyes, and W. M. L. Morawitz (1999), The California Current System in the Southern California Bight and the Santa Barbara Channel, *J. Geophys. Res.*, *104*(C4), 7659–7714.

Brink, K. H. (1982), A comparison of long coastal trapped wave theory with observations off Peru, *J. Phys. Oceanogr.*, *12*, 897–913.

Brink, K. H. (1989), Energy conservation in coastal-trapped wave calculations, *J. Phys. Oceanogr.*, *19*, 1011–1016.

Brink, K. H. (1990), On the damping of free coastal-trapped waves, *J. Phys. Oceanogr.*, *20*, 1219–1225.

Brink, K. H. (1991), Coastal-trapped waves and wind-driven currents over the continental shelf, *Annu. Rev. Fluid Mech.*, *23*, 389–412.

Brink, K. H. (2006), Coastal-trapped waves with finite bottom friction, *Dyn. Atmos. Oceans*, *41*, 172–190.

Brink, K. H., and D. C. Chapman (1987), Programs for computing properties of coastal-trapped waves and wind-driven motions over the continental shelf and slope, Tech. Rep. WHOI-87-24, Woods Hole Oceanogr. Inst., Woods Hole, Mass.

Brink, K. H., and R. D. Muench (1986), Circulation in the point conception-Santa Barbara channel region, *J. Geophys. Res.*, *91*(C1), 877–895.

Brink, K. H., D. W. Stuart, and J. C. van Leer (1984), Observations of the coastal upwelling region near 34°30′N off California: Spring 1981, *J. Phys. Oceanogr.*, *14*(2), 378–391.

Brink, K. H., D. C. Chapman, and G. R. Halliwell Jr. (1987), A stochastic model for wind-driven currents over the continental shelf, *J. Geophys. Res.*, *92*(C2), 1783–1797.

Chapman, D. C. (1987), Application of wind-forced, long, coastal-trapped wave theory along the California coast, *J. Geophys. Res.*, *92*(C2), 1798–1816.

Charney, J. G. (1955), The generation of ocean currents by wind, *J. Mar. Res.*, *14*, 477–498.

Chelton, D. B. (1984), Seasonal variability of alongshore geostrophic velocity off central California, *J. Geophys. Res.*, *89*(C3), 3473–3486.

Chelton, D. B., and D. B. Enfield (1986), Ocean signals in tide gauge records, *J. Geophys. Res.*, *91*(B9), 9081–9098.

Chelton, D. B., A. W. Bratkovich, R. L. Bernstein, and P. M. Kosro (1988), Poleward flow off central California during the spring and summer of 1981 and 1984, *J. Geophys. Res.*, *93*(C9), 10,604–10,620.

Chelton, D. B., R. A. DeSzoeke, M. G. Schlax, K. E. Naggar, and N. Siwertz (1998), Geophysical variability of the first baroclinic Rossby radius of deformation, *J. Phys. Oceanogr.*, *28*, 433–460.

Clarke, A., and K. Brink (1985), The response of stratified, frictional flow of shelf and slope waters to fluctuating large-scale, low-frequency wind forcing, *J. Phys. Oceanogr.*, *15*(4), 439–453.

Clarke, A. J. (1977), Observational and numerical evidence for wind-forced coastal trapped long waves, *J. Phys. Oceanogr.*, *7*, 231–247.

Clarke, A. J. (1982), Low-frequency reflection from a nonmeridional Eastern ocean boundary and the use of coastal sea level to monitor Eastern Pacific Equatorial Kelvin waves, *J. Phys. Oceanogr.*, *22*, 163–183.

Clarke, A. J. (1983), The reflection of equatorial waves from oceanic boundaries, *J. Phys. Oceanogr.*, *13*, 1193–1207.

Clarke, A. J., and C. Shi (1991), Critical frequencies at ocean boundaries, *J. Geophys. Res.*, *96*(C6), 10,731–10,738.

Collins, C. A., N. Garfield, R. G. Paquette, and E. Carter (1996), Lagrangian measurement of subsurface poleward flow between 38°N and 43°N along the West coast of the United States during summer, 1993, *Geophys. Res. Lett.*, *23*(18), 2461–2464.

Csanady, G. T. (1982), *Circulation in the Coastal Ocean*, 279 pp., D. Reidel, Boston, USA.

Davis, A. (1983), Shelf similar topographies for free continental shelf waves, *Geophys. Astrophys. Fluid Dyn.*, *23*(4), 321–331, doi:10.1080/03091928308209048.

Davis, R. E., and P. S. Bogden (1989), Variability on the California shelf forced by local and remote winds during the Coastal Ocean Dynamics Experiment, *J. Geophys. Res.*, *94*(C4), 4763–4783.

Davis, R. E., M. D. Ohman, D. L. Rudnick, J. T. Sherman, and B. Hodges (2008), Glider surveillance of physics and biology in the southern California Current System, *Limnol. Oceanogr.*, *53*(5), 2151–2168.

Denbo, D. W., and J. S. Allen (1987), Large-scale response to atmospheric forcing of shelf currents and coastal sea level off the West coast of North America: May-July 1981 and 1982, *J. Geophys. Res.*, *92*(C2), 1757–1782.

Dorman, C. E., and C. D. Winant (1995), Buoy observations of the atmosphere along the West coast of the United States, 1981–1990, *J. Geophys. Res.*, *100*(C8), 16,029–16,044.

Ebisuzaki, W. (1997), A method to estimate the statistical significance of a correlation when the data are serially correlated, *J. Clim.*, *10*(9), 2147–2153.

Emery, W. J., and R. E. Thomson (1997), Data Analysis Methods in Physical Oceanography, 634 pp., Elsevier, Boston, USA.

Fandry, C. B., L. M. Leslie, and R. J. Steedman (1984), Kelvin-type coastal surges generated by tropical cyclones, *J. Phys. Oceanogr.*, *14*(3), 582–593.

Fjeldstad, J. E. (1933), Interne wellen, *Geofys. Publ.*, *10*(6), 1–35.

Gan, J., and J. S. Allen (2002), A modeling study of shelf circulation off northern California in the region of the Coastal Ocean Dynamics Experiment: Response to relaxation of upwelling winds, *J. Geophys. Res.*, *107*(C9), 3123, doi:1029/2000JC000768.

García-Reyes, M., and J. L. Largier (2010), Observations of increased wind-driven coastal upwelling off central California, *J. Geophys. Res.*, *115*, C04011, doi:10.1029/2009JC005576.

Garfield, N., C. A. Collins, R. G. Paquette, and E. Carter (1999), Lagrangian exploration of the California Undercurrent, 1992-95, *J. Phys. Oceanogr.*, *29*, 560–583.

Garfield, N., M. E. Maltrud, C. A. Collins, T. A. Rago, and R. G. Paquette (2001), Lagrangian flow in the California Undercurrent, an observation and model comparison, *J. Mar. Syst.*, *29*, 201–220.

Gay, P. S., and T. K. Chereskin (2009), Mean structure and seasonal variability of the poleward undercurrent off southern California, *J. Geophys. Res.*, *114*, C02007, doi:10.1029/2008JC004886.

Gill, A., and E. Schumann (1974), The generation of long shelf waves by the wind, *J. Phys. Oceanogr.*, *4*(1), 83–90.

Grimshaw, R., and J. S. Allen (1988), Low-frequency baroclinic waves off coastal boundaries, *J. Phys. Oceanogr.*, *18*, 1124–1143.

Halliwell, G. R., Jr., and J. S. Allen (1984), Large-scale sea level response to atmospheric forcing along the West Coast of North America, Summer 1973, *J. Phys. Oceanogr.*, *14*, 864–886.

Hickey, B. M. (1998), Coastal oceanography of western North America from the tip of Baja California to Vancouver Island, in The Sea: The Global Coastal Ocean, vol. *11*, chap. *12*., pp. 345–393, John Wiley, New York, USA.

Hickey, B. M., and N. E. Pola (1983), The seasonal alongshore pressure gradient on the West Coast of the United States, *J. Geophys. Res.*, *88*(C12), 7623–7633.

Hickey, B. M., E. L. Dobbins, and S. E. Allen (2003), Local and remote forcing of currents and temperature in the central Southern California Bight, *J. Geophys. Res.*, *108*(C3), 3081, doi:10.1029/2000JC000313.

Huyer, A. (1990), The offshore structure and subsurface expression of sea level variations off Peru, 1976–1977, *J. Phys. Oceanogr.*, *10*, 1755–1768.

Huyer, A., and R. L. Smith (1985), The signature of El Nino off Oregon, 1982–1983, *J. Geophys. Res.*, *90*(C4), 7133–7142.

Huyer, A., P. M. Kosro, S. J. Lentz, and R. C. Beardsley (1989), Poleward flow in the California Current System, in Poleward Flows Along Eastern Ocean Boundary*, Coastal and Estuarine Studies*, vol. 34, pp. 142–156, Springer, New York, USA.

Kaplan, D. M., J. L. Largier, and L. W. Botsford (2005), HF radar observations of surface circulation off Bodega Bay (northern California, USA), *J. Geophys. Res.*, *110*, C10020, doi:10.1029/2005JC002959.

Kim, S. Y. (2010), Observations of submesoscale eddies using high-frequency radar-derived kinematic and dynamic quantities, *Cont. Shelf Res.*, *30*, 1639–1655, doi:10.1016/j.csr.2010.06.011.

Kim, S. Y. (2013), A statistical description on the wind-coherent responses of sea surface heights off the U.S. West Coast, *Ocean Dynamics*, doi:10.1007/s10236-013-0668-3.

Kim, S. Y., and P. M. Kosro (2013), Observations of near-inertial surface currents off Oregon: Decorrelation time and length scales, *J. Geophys. Res.*, *118*, 3723–3736, doi:10.1002/jgrc.20235.

Kim, S. Y., E. J. Terrill, and B. D. Cornuelle (2008), Mapping surface currents from HF radar radial velocity measurements using optimal interpolation, *J. Geophys. Res.*, *113*, C10023, doi:10.1029/2007JC004244.

Kim, S. Y., B. D. Cornuelle, and E. J. Terrill (2009a), Anisotropic response of surface currents to the wind in a coastal region, *J. Phys. Oceanogr.*, *39*(6), 1512–1533, doi:10.1175/2009JPO4013.1.

Kim, S. Y., E. J. Terrill, and B. D. Cornuelle (2009b), Assessing coastal plumes in a region of multiple discharges: The U.S.–Mexico border, *Environ. Sci. Technol.*, *43*(19), 7450–7457, doi:10.1021/es900775p.

Kim, S. Y., B. D. Cornuelle, and E. J. Terrill (2010a), Decomposing observations of high-frequency radar derived surface currents by their forcing mechanisms: Decomposition techniques and spatial structures of decomposed surface currents, *J. Geophys. Res.*, *115*, C12007, doi:10.1029/2010JC006222.

Kim, S. Y., B. D. Cornuelle, and E. J. Terrill (2010b), Decomposing observations of high-frequency radar derived surface currents by their forcing mechanisms: Locally wind-driven surface currents, *J. Geophys. Res.*, *115*, C12046, doi:10.1029/2010JC006223.

Kim, S. Y., et al. (2011), Mapping the U.S. West Coast surface circulation: A multiyear analysis of high-frequency radar observations, *J. Geophys. Res.*, *116*, C03011, doi:10.1029/2010JC006669.

Kosro, P. M. (1987), Structure of the coastal current field off Northern California during the Coastal Ocean Dynamics Experiement, *J. Geophys. Res.*, *92*(C2), 1637–1654.

Kosro, P. M. (2002), A poleward jet and an equatorward undercurrent observed off Oregon and northern California, during the 1997-98 El Nino, *Prog. Oceanogr.*, *54*, 343–360.

Kosro, P. M. (2005), On the spatial structure of coastal circulation off Newport, Oregon, during spring and summer 2001 in a region of varying shelf width, *J. Geophys. Res.*, *110*, C10S06, doi:10.1029/2004JC002769.

Kosro, P. M., et al. (1991), The structure of the transition zone between coastal waters and the open ocean off northern California, winter and spring 1987, *J. Geophys. Res.*, *96*(C8), 14,707–14,730.

Largier, J. L., B. A. Magnell, and C. D. Winant (1993), Subtidal circulation over the northern California shelf, *J. Geophys. Res.*, *98*(C10), 18,147–18,179.

Lavin, M. F., E. Beier, J. Gomez-Valdes, V. M. Godinez, and J. Garcia (2006), On the summer poleward coastal current off SW Mexico, *Geophys. Res. Lett.*, *33*, L02601, doi:10.1029/2005GL024686.

Lynn, R. J., and J. J. Simpson (1987), The California Current System: The seasonal variability of its physical characteristics, *J. Geophys. Res.*, *92*(C12), 12,947–12,966.

Marchesiello, P., J. C. McWilliams, and A. Shchepetkin (2003), Equilibrium structure and dynamics of the California Current System, *J. Phys. Oceanogr.*, *33*, 753–783.

McCreary, J. P., Jr., P. K. Kundu, and S.-Y. Chao (1987), On the dynamics of the California Current System, *J. Mar. Res.*, *45*, 1–32.

Miles, J. W. (1972), Kelvin waves on oceanic boundaries, *J. Fluid Mech.*, *55*(1), 113–127.

Paduan, J. D., and M. S. Cook (1997), Mapping surface currents in Monterey Bay with CODAR-type HF radar, *Oceanography*, *10*, 49–52.

Pierce, S. D., R. L. Smith, P. M. Kosro, J. A. Barth, and C. D. Wilson (2000), Continuity of the poleward undercurrent along the Eastern boundary of the mid-latitude north Pacific, *Deep Sea Res., Part II*, *47*, 811–829.

Pringle, J., and E. Dever (2009), Dynamics of wind-driven upwelling and relaxation between Monterey Bay and Point Arena: Local-, regional-, and gyre-scale controls, *J. Geophys. Res.*, *114*, C07003, doi:10.1029/2008JC005016.

Ramp, S. R. (1989), Review and commentary to poleward flows in the California Current System*, in Poleward Flows Along Eastern Ocean Boundary, Coastal and Estuarine Studies*, vol. 34, edited by A. Huyer et al., pp. 157–159, Springer, New York, USA.

Ramp, S. R., L. K. Rosenfeld, T. D. Tisch, and M. R. Hicks (1997), Moored observations of the current and temperature structure over the continental shelf off central California: 1. A basic description of the variability, *J. Geophys. Res.*, *102*(C10), 22,877–22,902.

Reid, J. L., and R. A. Schwartzlose (1962), Direct measurements of the Davidson Current off central California, *J. Geophys. Res.*, *67*, 2491–2497.

Rhines, P. (1970), Edge-, bottom-, and Rossby waves in a rotating stratified fluid, *Geophys. Fluid Dyn.*, *1*, 273–302.

Robinson, A. R. (1964), Continental shelf waves and the response of sea level to weather systems, *J. Geophys. Res.*, *69*(2), 367–368.

Shay, L. K. (1997), Internal wave-driven surface currents from HF radar, *Oceanography*, *10*(2), 60–63.

Smith, R. L. (1983), Peru coastal current during El Nino: 1976 and 1982, *Science*, *221*, 1379–1399.

Spillane, M. C., D. B. Enfield, and J. S. Allen (1987), Intraseasonal oscillations in sea level along the West coast of the Americas, *J. Phys. Oceanogr.*, *17*(3), 313–325.

Stammer, D. (1997), Global characteristics of ocean variablity estimated from regional TOPEX/POSEIDON altimeter measurements, *J. Phys. Oceanogr.*, *27*(8), 1743–1769.

Steger, J. M., F. B. Schwing, C. A. Collins, L. K. Rosenfeld, N. Garfield, and E. Gezgin (2000), The circulation and water masses in the Gulf of the Farallones, *Deep Sea Res. Part II*, *47*, 907–946.

Strub, P. T., and C. James (2000), Altimeter-derived variability of surface velocities in the California Current System: 2. Seasonal circulation and eddy statistics, *Deep Sea Res., Part II*, *47*, 831–870.

Sverdrup, H. U., M. W. Johnson, and R. H. Fleming (1942), *The Oceans*, 1060 pp., Prentice Hall, Englewood Cliffs, N. J.

Tang, Y. M., and R. Grimshaw (1995), A model analysis of coastally trapped waves generated by tropical cyclone, *J. Phys. Oceanogr.*, *25*(7), 1577–1598.

U.S. Department of Commerce, National Oceanic and Atmospheric Administration, National Geophysical Data Center, 2006. 2-minute Gridded Global Relief Data (ETOPO2v2), National Geophysical Data Center, National Oceanic and Atmospheric Administration, U.S. Department of Commerce, Washington, D.C.

Wang, D.-P., and C. N. K. Mooers (1976), Coastal-trapped waves in a continuously stratified ocean, *J. Phys. Oceanogr.*, *6*, 853–863.

Washburn, L., M. R. Fewings, C. Melton, and C. Gotschalk (2011), The propagating response of coastal circulation due to wind relaxations along the central California coast, *J. Geophys. Res.*, *116*, C12028, doi:10.1029/2011JC007502.

Webster, I. (1987), Scattering of coastally trapped waves by changes in continental shelf width, *J. Phys. Oceanogr.*, *17*(7), 928–937.

Wichham, J. B., A. A. Bird, and C. N. K. Mooers (1987), Mean and variable flow over the central California continental margin, 1978–1980, *Cont. Shelf Res.*, *7*(8), 827–849.

Wilkin, J., and D. Chapman (1987), Scattering of continental shelf waves at a discontinuity in shelf width, *J. Phys. Oceanogr.*, *17*(6), 713–724.

Wilkin, J. L., and D. C. Chapman (1990), Scattering of coastal-trapped waves by irregularities in coastline and topography, *J. Phys. Oceanogr.*, *20*, 396–421.

Wing, S. R., J. L. Largier, L. W. Botsford, and J. F. Quinn (1995), Settlement and transport of benthic invertebrates in an intermittent upwelling region, *Limnol. Oceanogr.*, *40*(2), 316–329.

Wunsch, C., and D. Stammer (1997), Atmospheric loading and the oceanic 'inverted barometer' effect, *Rev. Geophys.*, *35*(1), 79–107, doi:10.1029/96RG03037.

Yelland, M., and P. K. Taylor (1996), Wind stress measurements from the open ocean, *J. Phys. Oceanogr.*, *26*, 541–558.